MATERIALS SCIENCE

Few- and single-molecule reservoir computing experimentally demonstrated with surface-enhanced Raman scattering and ion gating

Daiki Nishioka[1,2], **Yoshitaka Shingaya**[1], **Takashi Tsuchiya**[1]*, **Tohru Higuchi**[2], **Kazuya Terabe**[1]

Molecule-based reservoir computing (RC) is promising for achieving low power consumption neuromorphic computing, although the information-processing capability of small numbers of molecules is not clear. Here, we report a few- and single-molecule RC that uses the molecular vibration dynamics in the para-mercaptobenzoic acid (pMBA) detected by surface-enhanced Raman scattering (SERS) with tungsten oxide nanorod/silver nanoparticles. The Raman signals of the pMBA molecules, adsorbed at the SERS active site of the nanorod, were reversibly perturbated by the application of voltage-induced local pH changes near the molecules, and then used to perform time-series analysis tasks. Despite the small number of molecules used, our system achieved good performance, including >95% accuracy in various nonlinear waveform transformations, 94.3% accuracy in solving a second-order nonlinear dynamic system, and a prediction error of 25.0 milligrams per deciliter in a 15-minute-ahead blood glucose level prediction. Our work provides a concept of few-molecular computing with practical computation capabilities.

INTRODUCTION

While artificial intelligence (AI) provides convenience in a variety of human activities through high-performance deep learning, the huge energy consumption and heavy communication traffic that accompanies the current cloud-based AI systems have become serious problems (*1*). Recently, in an effort to overcome the drawbacks of current AI systems, physical reservoir computing (PRC) has begun to attract attention (*2*, *3*). Conventional deep learning requires massive computation resources to handle the enormous networks they require [i.e., vast numbers of weights, stored and updated in the learning (training) process], while PRC is theoretically predicted to have comparable performance due to its harnessing of the inherent nonlinear responses of physical dynamical systems, termed “physical reservoirs” in the framework of reservoir computing (RC), for mapping time-series data to high-dimensional feature space to achieve efficient information processing (*4*, *5*). To the present, in the search for high-performance (high information-processing capability and low power consumption) PRC, lots of materials and devices [e.g., memristor, spintronics devices, soft bodies, nanowire networks (NWNs), optical circuits, and ionic devices] have been intensively explored and applied to a variety of pattern recognition and prediction tasks, including nonlinear transformation tasks, handwritten digit recognition, and face classification (*2*, *3*, *5*–*39*). While the best computational performance and robustness in information processing have been demonstrated with nonlinear optical circuits (*19*–*21*), making PRC particularly attractive for next-generation leading-edge AI systems, one serious problem has arisen; notably, the larger volume compared to the volumes found in semiconductor reservoir elements/arrays (*2*, *3*, *12*–*33*). The nonlinear optical circuits require bulky optical fiber in lengths as long as several kilometers to perform PRC, resulting in a large physical volume of reservoirs and limited integration (*19*–*21*).

In this regard, a small number of molecules, with an extremely small volume, is a promising candidate for the realization of high computational performance and highly integrated PRC, which would lead to its implementation in electronic devices. The concept of molecular RC was previously proposed, and there have been a few reports of work on theoretical simulations and experimental demonstrations with preliminary tasks (*25*–*37*). However, the number of molecules in the reported works was quite numerous in each case [e.g., a network of single-walled carbon nanotubes (CNTs) complexed with polyoxometalate (POM) (*25*, *26*), organic dendritic networks composed of the semiconductor PEDOT:PF6 (*27*, *28*), a sulfonated polyaniline network (*29*), a p-NDI transistor (*30*), an electrochemical cell using ionic liquid (*31*, *32*) and a POM molecule in the solution (*33*), a Polymerase-Exonuclease-Nickase Dynamic Network Assembly toolbox (*34*), a gene regulation network with mRNA (*35*), and a deoxyribozyme oscillator with DNA molecules (*36*)]. The number of molecules in the experimentally demonstrated reservoirs is numerous, although the physical volume of these conventional molecular approaches is commensurate with the dimensions of the digital complementary metal-oxide semiconductor. Therefore, to date, the feasibility of single to few molecular RC with practical tasks is unclear since the macroscopic response from nonlinear dynamics of a large number of molecules was used for reservoir computation (*36*). In particular, it is not straightforward to track the nonlinear dynamics of a few molecules sufficiently precisely to enable PRC. By tracking the nonlinear dynamics of a small number of molecules accurately, the microscopic dynamics of molecules can be used for information processing. As a result, new information processing devices will be achieved by selecting and integrating various molecules according to the desired task or application. Such an approach is expected to ultimately prove useful in the design of next-generation architectures that integrate sensing and information processing.

Here, we demonstrate a few-molecule RC (FM-RC) using the molecular vibration dynamics in para-mercaptobenzoic acid (pMBA). The molecular dynamics of approximately one to four pMBA molecules was detected by surface-enhanced Raman scattering (SERS) with tungsten oxide nanorod/silver nanoparticles (WO_x@Ag-NPs)

---

[1] Research Center for Materials Nanoarchitectonics (MANA), National Institute for Materials Science (NIMS), 1-1 Namiki, Tsukuba, Ibaraki 305-0044, Japan. [2] Department of Applied Physics, Faculty of Science, Tokyo University of Science, 6-3-1 Niijuku, Katsushika, Tokyo 125-8585, Japan.
*Corresponding author. Email: tsuchiya.takashi@nims.go.jp

(*40*). To perform RC of standard benchmark tasks, the Raman signal of the pMBA molecules, adsorbed at the SERS active site of WO_x@Ag-NPs, was reversibly perturbated by applied voltage-induced local pH changes in the vicinity of the molecules (*41*–*45*). Despite only a few molecules being present, our system achieved good performance accuracy (95.1 to 97.7%) in various nonlinear waveform transformations and 94.3% accuracy in a second-order nonlinear transformation task. Furthermore, our system achieved good prediction performance in the 15-min-ahead prediction task for blood glucose levels, with a root mean square error (RMSE) of 25.0 mg/dl for four molecules and 42.1 mg/dl for a single molecule. This task has rarely been demonstrated in PRC, and our system achieved the best prediction performance in PRC (*39*). Our results open up a solid new direction for molecular computing, which combines the high integration potential offered by a few molecules of nonlinear elements with practical computational power for pattern recognition and prediction tasks (*36*, *46*–*51*).

RESULTS

The molecular vibrations of a few molecules were detected using the very large SERS effect of conductive tungsten oxide (WO_x) (*40*). Figure 1A shows a schematic diagram of the experimental arrangement for the subject Raman scattering measurements, in an electrochemical system. A single WO_x nanorod was fixed, with epoxy resin, to the apex of a sharpened tungsten tip, as shown in fig. S1. The tip was inserted into the meniscus of the electrolyte solution formed between a 100× immersion objective lens and a petri dish, following which a laser beam was irradiated to the center of the WO_x nanorod. Voltage was applied to the WO_x nanorod in the electrochemical arrangement shown in Fig. 1A. The tungsten-tipped WO_x nanorod was used as the working electrode, and a platinum wire was used as the counter and pseudo-reference electrode. Figure 1B is an optical microscope image of the WO_x nanorods observed in an aqueous electrolyte solution. The WO_x nanorods used here have a {001} type crystallographic shear (CS) structure in the crystal and exhibit metallic electrical conduction properties (*52*–*54*). One of the authors previously reported that WO_x nanorods with this type of crystalline structure exhibit a very large Raman enhancement effect and can be used for single-molecule Raman detection (*40*). It is thought that a large enhancement effect can be obtained by introducing defects into the CS structure and forming a nanogap on the conducting plane. In this study, in addition to introducing such defects on the conducting plane of the WO_x nanorods, a small number of silver nanoparticles were attached to the WO_x nanorods to form a nanogap between the WO_x nanorods and the silver nanoparticles, so as to obtain an additional enhancement effect. This method is suitable for observing Raman scattering of adsorbed molecules from electrolyte solutions because it more reliably forms a SERS active site on the WO_x nanorod surface. In Fig. 1B, the central area of the WO_x nanorods appears brighter. Silver nanoparticles are electrodeposited in this region and form a SERS active site. Since electrodeposition on WO_x nanorods occurs at the light-irradiated area, it is possible to control the position at which the silver particles are attached. Figure 1C is a transmission electron microscopy (TEM)

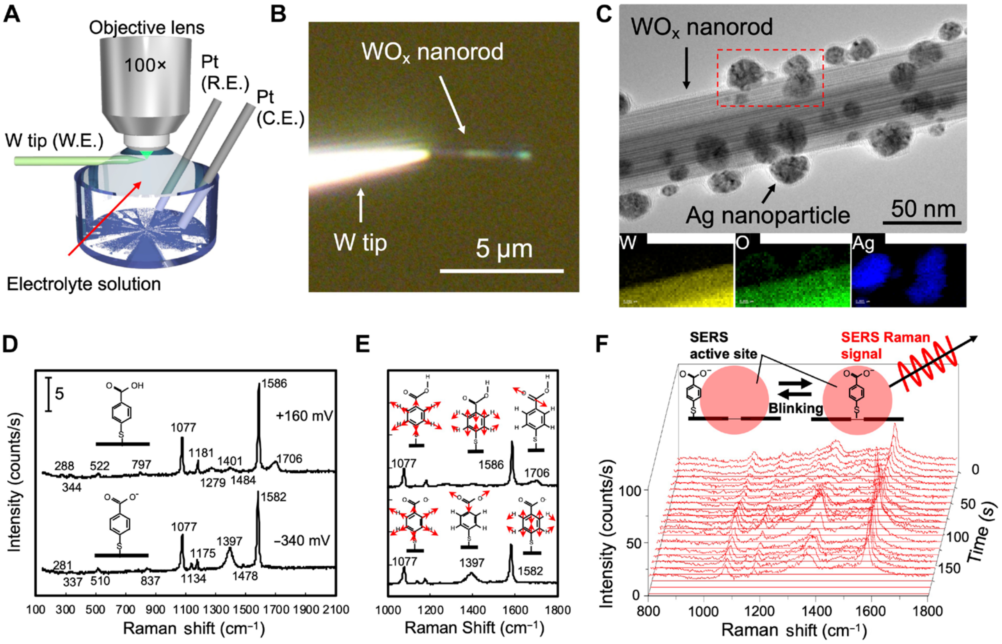

Fig. 1. SERS measurement of pMBA molecules at a silver nanoparticle–modified WO_X nanorod. (**A**) Schematic diagram of laser irradiation and electrode arrangement for SERS measurements. (**B**) Optical microscope image of a WO_x nanorod attached at the apex of a tungsten tip. (**C**) Transmission electron microscopy image of a WO_x nanorod modified with silver nanoparticles. The three images at the bottom of the figure represent energy-dispersive x-ray spectroscopy (EDS) maps of the area enclosed by the red dotted square in the TEM image. The three images represent EDS maps of tungsten, oxygen, and silver, respectively. (**D**) SERS spectra obtained from Ag nanoparticle–modified WO_x nanorod in a 0.15 M NaCl aqueous solution. The pMBA concentration was 10 μM, the excitation laser wavelength was 488 nm, and the laser power was 20 μW. (**E**) Schematic diagram of vibrational modes corresponding to the peaks appearing at 1077, 1586, and 1706 cm^{-1} of protonated pMBA and at 1077, 1397, and 1582 cm^{-1} of deprotonated pMBA. (**F**) Time-resolved SERS spectra obtained from WO_x nanorod modified with silver nanoparticles. The pMBA concentration was 1 nM.

image of tungsten oxide nanorods in the area where the silver particles were electrodeposited. It can be seen that the silver nanoparticles, 5 to 30 nm in diameter, have become attached to the WO_x nanorod.

Figure 1D is the Raman scattering spectra of a silver nanoparticle–modified WO_x nanorod, obtained in a 0.15 M NaCl solution with 10 μM pMBA. The structure of the pMBA molecule changes with the pH in the carboxyl groups, which difference is clearly shown in the Raman spectra and which makes it possible for it to be used for local pH sensing (*41*–*45*). In the present study, changes in electrode potential provide spectral changes comparable to those obtained by changing pH. At +160 mV versus standard hydrogen electrode (SHE), a ν(C=O) peak appears at 1706 cm^{-1}, indicating that the carboxyl groups of the adsorbed molecules are protonated. In contrast, the 1706 cm^{-1} peak disappears completely at −340 mV versus SHE and a $\nu(COO^-)$ peak appears at 1397 cm^{-1}, which indicates that the carboxyl groups of pMBA are deprotonated. Figure 1E is a schematic diagram of vibrational modes corresponding to the peaks that appeared at 1077, 1586, and 1706 cm^{-1} of protonated pMBA and at 1077, 1397, and 1582 cm^{-1} of deprotonated pMBA (*55*–*57*). The peaks at 1077 cm^{-1} were assigned to a ring breathing mode and a ν(C-S) mode. The peaks at 1586 and 1582 cm^{-1} were assigned to a ring stretching mode. FM-RC uses such potential-dependent molecular vibrational behavior of only a few molecules as a computational resource for information processing. Unlike conventional methods that use the macroscopic network structure and electrical properties formed by a vast number of organic molecules as a computational resource, our approach takes advantage of the information processing capability of the microscopic nonlinear behavior of a few molecules. Figure 1F shows the time-resolved SERS spectra of a silver nanoparticle–modified WO_x nanorod, obtained by reducing the concentration of pMBA to 1 nM. Characteristic blinking phenomena are exhibited when observing extremely small amounts of molecules at the single-molecule level. Such blinking phenomena are a widely accepted feature of the SERS spectra of single molecules (*40*, *58*–*60*). This phenomenon is due to the presence of only a single molecule in the nanogap, which is an extremely small SERS active site (*40*, *58*–*60*). Therefore, it can be concluded that the present system, in which silver particles are electrodeposited on WO_x nanorods, provides a very large enhancement effect that enables single-molecule detection.

The number of molecules in this system was calculated by comparing the intensity of the Raman peaks in a pMBA solution with a concentration of 1 nM, which is capable of single-molecule detection, and a pMBA solution with a concentration of 10 μM, which is capable of few-molecule detection. Figure S2 shows the SERS spectra corresponding to the ring stretching mode of pMBA for single and few molecules. To eliminate variations in the enhancement effect from sample to sample, the SERS spectra of single molecules were measured with 1 nM pMBA, and then the Raman spectra of a few molecules were measured by increasing the pMBA concentration to 10 μM. The ratio of the integrated intensities of each SERS spectra was 1:4, thus the SERS spectrum at 10 μM pMBA reflects about four pMBA molecules.

Nonlinear waveform transformation task

A nonlinear waveform transformation (regression) task (*8*, *16*, *18*, *24*) was performed to demonstrate the computational capability of the FM-RC. Figure 2A is a schematic of the task calculated by the FM-RC. The goal of this task is to generate sin wave (Sin), square wave (Square), π/2 phase-shifted triangular wave (Shift), and frequency-doubled triangular wave (2f) by the linear combination (Eq. 1) of readout weights $\boldsymbol{W}$ and the reservoir states $\boldsymbol{X}$ (in this case Raman spectrum) to the triangular wave input

$$\boldsymbol{Y}(k) = \boldsymbol{W}\boldsymbol{X}(k) \tag{1}$$

where k and $\boldsymbol{Y}(k)$ are the discrete time step and reservoir output, respectively. The input triangular wave $u(k)$ and each target waveform $\boldsymbol{T}(k)$ to be generated by the reservoir are shown in fig. S3. This task requires nonlinearity and high dimensionality in the reservoir, by which the basic computational capability of the reservoir can be evaluated. The input triangular wave for the nonlinear waveform transformation task was converted into a voltage signal of 10 seconds per step (0.1 Hz) and 20 steps per period, and input to the WO_x nanorod working electrode on which the pMBA molecule was adsorbed. This was done in the range of −340 to +160 mV versus SHE as shown in fig. S4. The Raman spectral response with 10 μM pMBA for time steps to the periodic triangular wave input is shown in Fig. 2B. It can be seen that the bright SERS bands including $\nu(COO^-)$ peak at 1384 cm^{-1} and ν(C=O) peak at 1693 cm^{-1} (*41*, *42*) exhibit periodic blinking by responding to the triangular wave input. This is due to the applied voltage-induced reversible protonation and deprotonation of the carboxyl groups of pMBA, as shown in Fig. 1D. Two hundred reservoir states were obtained from these Raman spectra, uniformly in the range of 945 to 1728 cm^{-1}. This means that not only the reversible and independent nonlinear dynamics of the prominent peaks corresponding to the ring-breathing mode and the ν(C-S) mode (1077 cm^{-1}), the ring-stretching mode (1582 to 1586 cm^{-1}), but also the reversible and independent nonlinear dynamics of the minor structures shown in Fig. 1E corresponding to $\nu(COO^-)$ mode (1397 cm^{-1}) and ν(C=O) (1706 cm^{-1}) contribute to perform the task. The readout weights were stored in a personal computer and trained by ridge regression so that the reservoir output $\boldsymbol{Y}$(k), obtained by the linear combination of reservoir states and weights, agreed with the target waveform $\boldsymbol{T}(k)$. Details of the method and learning algorithm are given in Materials and Methods.

Figure 2C shows the target waveform and the output waveform from the molecule reservoir for each transformation task. For all tasks, the FM-RC generates waveforms that are in good agreement with the target waveforms, which means that the voltage response of only a few pMBA molecules has the capability of performing nonlinear transformations that can be used for information processing in RC. The subject FM-RC achieved 97.6% accuracy ($MSE = 2.91 \times 10^{-4}$) for "Sin," 95.1% ($MSE = 2.42 \times 10^{-3}$) for "Square," 97.7% ($MSE = 1.74 \times 10^{-4}$) for "Shift," and 97.1% ($MSE = 3.00 \times 10^{-4}$) for "2f" in each conversion task. Whereas the performance for the Sin task was comparable to other physical reservoirs, the subject FM-RC outperformed a yttria-stabilized zirconia/diamond-based electric double-layer ion-gating reservoir (EDL-IGR) and NWN reservoirs for the other tasks, as shown in Fig. 2D and Table 1 (*8*, *16*, *18*, *24*). In particular, the FM-RC achieved excellent accuracy of as high as 97.1% for the 2f task, which the task requires the strongest and most complex variety of nonlinearities among the four transformation tasks, which NWN reservoirs could thus only solve under extremely limited conditions that were tuned to an "edge of chaos" state (*16*) that maximizes the information processing capabilities as a dynamical system (*61*, *62*). In addition, for EDL-IGR (*24*), which performed the 2f task with the same high accuracy as FM-RC, the synaptic response based on ion-electron coupling dynamics was reported to be in an edge of

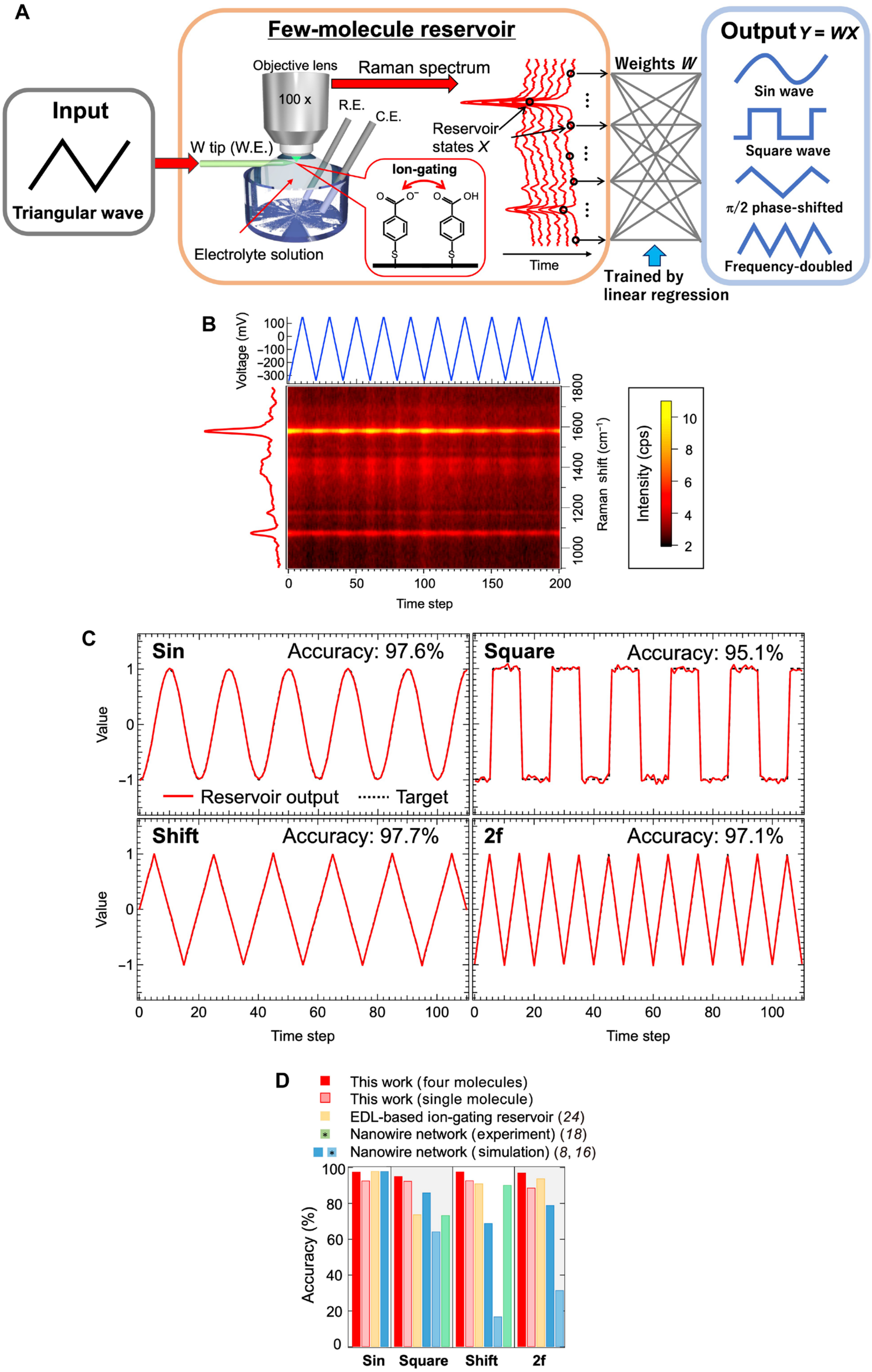

Fig. 2. Nonlinear waveform transformation task. (**A**) Schematic of the nonlinear waveform transformation task calculated by FM-RC. (**B**) Response of Raman spectra to triangular wave voltage application. (**C**) Results of the waveform transformation task using a sine wave, a square wave, a phase-shifted triangular wave, and a frequency-doubled triangular wave as the target waveform. The red line indicates the reservoir output and the black dotted line indicates the target waveform. (**D**) Comparison of the accuracy of the waveform transformation task with other physical reservoirs (*8*, *16*, *18*, *24*). Results of NWN, with sin wave used as input indicated by * (*8*, *18*).

Table 1. Comparison of the accuracy of the waveform transformation task with other physical reservoirs (*8*, *16*, *18*, *24*).

Task	This work (four molecules)	This work (single molecule)	EDL-IGR[24]	NWN[18]	NWN[16]	NWN[8]
Sin	97.6%	92.7%	98.0%	-	>98%	-
Square	95.1%	92.5%	73.8%	73.42%	86%	64.3%
Shift	97.7%	92.8%	91.1%	90.28%	69%	16.9%
2f	97.1%	88.7%	93.9%	-	79%	31.6%

chaos state (*22*). The fact that FM-RC outperformed such complexity-exhibiting PRC indicates the good nonlinearity and complexity of the subject FM-RC. In the nonlinear waveform transformation task, the extent of the nonlinearity in the physical reservoir dynamics is mainly reflected in the transformation accuracy. The present result evidences that reversible protonation and deprotonation of pMBA, caused by the local pH change, owns strong nonlinearity that is comparable to that exhibited by the electrical response of an atomic switch NWN, which is itself accompanied by collective resistive switching at numerous cross points in the network (*8*, *16*, *18*). Furthermore, the result supports the contention that the SERS technique, using a silver nanoparticle–modified WO_x nanorod, is capable of detecting the nonlinear response of few-molecule pMBA with a sufficient signal-to-noise ratio due to its excellent sensitivity. We also performed this task using single-molecule Raman spectra based on 1 nM pMBA. As shown in fig. S5, the target and predicted waveforms are in good agreement even with the single-molecule Raman spectra. As shown in Fig. 2D and Table 1, the single-molecule RC was slightly less accurate than the FM-RC for each task but achieved higher accuracy than most of the other physical reservoirs (*8*, *16*, *18*, *24*). The slight decrease in performance compared to the few molecules could be attributed to increased signal noise because of lower peak intensities and lower high dimensionality resulting from the absence of some minor peaks. However, since this task does not require a larger high dimensionality in the reservoir, the performance degradation caused by the lower high dimensionality was limited.

The nonlinear waveform transformation task corresponds to the Fourier decomposition of each signal (*16*). To convert to a sine wave, higher-order harmonics must be removed from the triangular wave input signal, and to convert to a square wave, an additional odd number of higher-order harmonics are required. In double-frequency conversion, odd higher-order harmonics must be removed and even harmonics must be added. In the case of a phase-shift transform, the reservoir must be delayed with respect to the input signal. In other words, the coefficients of the cosine terms of the Fourier series become the coefficients of the sine terms. Therefore, the reservoir requires nonlinearity to perform these Fourier decompositions (*16*). In particular, for this task, which processes periodic signals, the reservoir is not required to have memory that spans the period. On the other hand, in addition to nonlinearity, RC requires short-term memory and high dimensionality, and these have a relatively small impact on the accuracy of the task. To investigate the versatility of the molecular reservoir for PRC tasks needing all three requirements (i.e., nonlinearity, short-term memory, and high dimensionality), a more difficult task was performed. This is discussed in the following section.

Solving a second-order nonlinear dynamic equation task

We evaluated the performance of the subject FM-RC with the more difficult task of solving a second-order nonlinear dynamic equation (*5*, *11*, *22*, *23*) since the previous waveform transformation task is relatively easy. Figure 3A is a schematic of the task calculated by the FM-RC. In this task, in the training phase, the readout weights are trained so that the reservoir output matches the second-order nonlinear equation shown in Eq. 2. Then, it tests to make sure that the reservoir outputs (Eq. 1) are the same as the target (Eq. 2) for the untrained data (test phase)

$$T(k) = 0.4T(k-1) + 0.4T(k-1)T(k-2) + 0.6u^3(k) + 0.1 \quad (2)$$

where $u(k)$ is a random input ranging from 0 to 0.5 based on uniform random distribution as shown in fig. S6A. The reservoir is required to have at least two steps of short-term memory and nonlinearity to express Eq. 2. A detailed explanation of the learning algorithm and dataset can be found in Materials and Methods and fig. S6. Figure 3B shows the reservoir output and the target waveform during the training phase. Both waveforms are in good agreement, and the molecule reservoir learned the second-order nonlinear equations with 94.5% accuracy (MSE $= 1.71 \times 10^{-4}$). In the test phase, a dataset different from the one used in training was input to the FM-RC, and its prediction output was compared to a target generated by Eq. 2. As shown in Fig. 3C, the target waveform and the predicted waveform of the FM-RC were in good agreement, even using a dataset that was different from the one used in training, and the FM-RC was able to predict the target waveform with an accuracy of 94.3% (MSE $= 1.66 \times 10^{-4}$). Figure 3D shows the performance of the subject FM-RC compared with other physical reservoirs reported to date. Although the performance exhibited was not as good as that of spin-torque oscillators (*11*) (theoretical calculation) and ion-gating reservoirs (IGRs) (*22*, *23*) which use semiconductor channels, the subject FM-RC, despite its extremely small reservoir volume, achieved similar computational performance as a memristor RC (*5*). This indicates that the nonlinear dynamics reflecting structural changes caused by local pH changes in just a few pMBA molecules, measured via SERS measurements, has sufficient expressive power and short-term memory, as a dynamical system, to solve Eq. 2. As discussed above, RC computational performance depends on the nonlinearity and high dimensionality of the physical reservoir as a dynamical system in addition to these features. The high dimensionality of a reservoir corresponds to the diversity of the system and is achieved by the existence of a large number of nodes that exhibit independently different behaviors. In a simulation reservoir, high dimensionality is achieved by increasing the reservoir size, but in the case of a physical reservoir, the reservoir states obtained from the physical system do not necessarily behave independently and differently. These characteristics were analyzed to investigate the

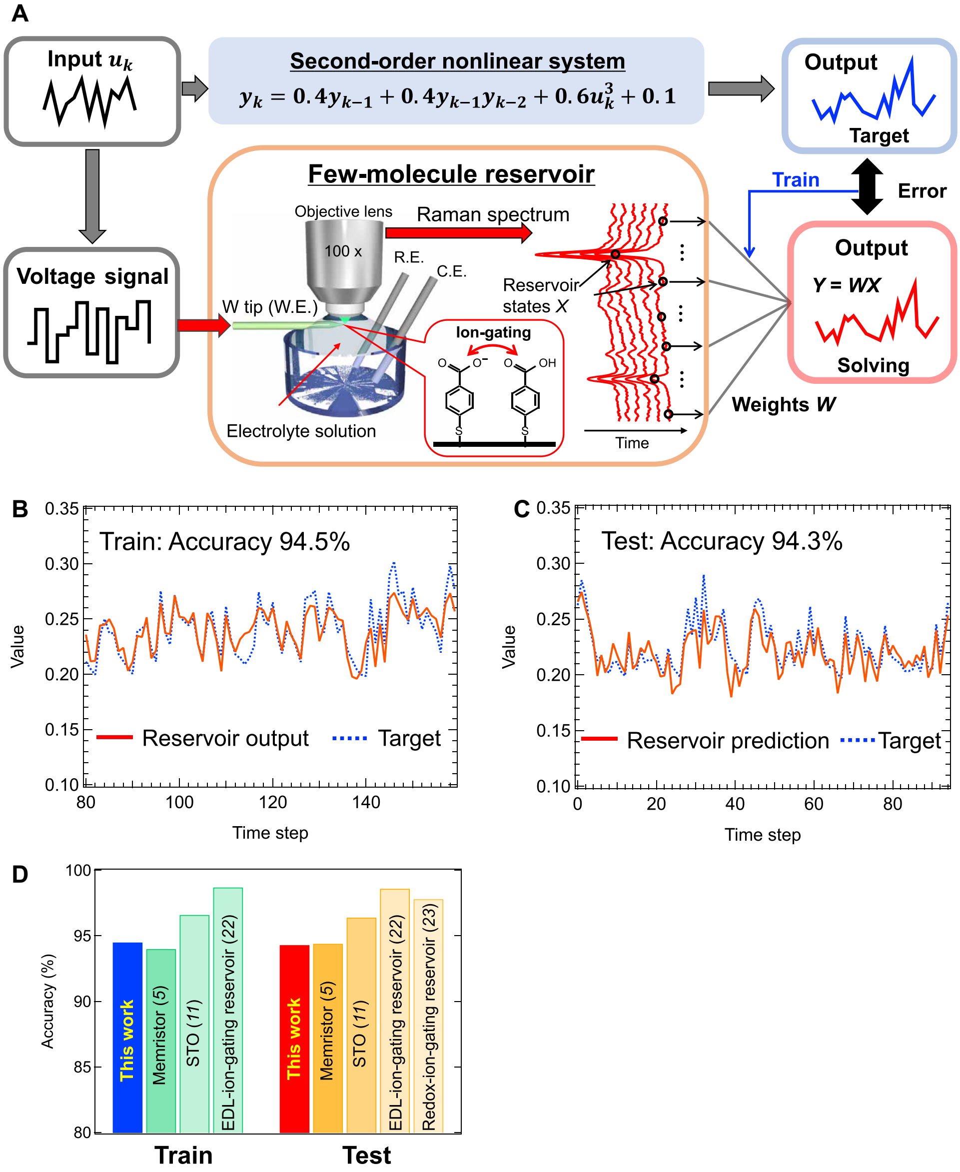

Fig. 3. Solving a second-order nonlinear dynamic equation task. (**A**) Schematic of task calculated by FM-RC. Target and prediction waveforms of the second-order nonlinear dynamic equation at the (**B**) train phase and (**C**) test phase. (**D**) Prediction accuracy compared to other physical reservoirs [memristor, spin-torque oscillator (STO), EDL-IGR, and redox type ion-gating reservoir] (*5*, *11*, *22*, *23*).

origin of the performance, as described in the following section. The power consumption of FM-RC is also discussed in section S1, fig. S11, and table S1.

Nonlinearity and high-dimensionality analysis of the few-molecule reservoir

We analyzed the origin of the computational capability of the FM-RC in terms of nonlinearity, which is a required property for reservoirs. In RC, the nonlinearity of the reservoir is directly related to the nonlinear information processing capability, and strong nonlinearity with respect to the input contributes substantially to the expressive power of the reservoir. Figure 4A shows the input voltage dependence of the reservoir states obtained from 1571 and 1587 cm^{-1}. The input-output characteristics of the reservoir state at 1587 cm^{-1} ($X_{1587\text{cm}^{-1}}$), corresponding to the peak top, are relatively linear, whereas the reservoir state at 1571 cm^{-1} ($X_{1571\text{cm}^{-1}}$) changes nonlinearly. This is attributed to the ring-stretching peak not only increasing in intensity as the input voltage decreases from +160 to −340 mV versus SHE but also shifting to the lower wave number side, as shown in the inset of Fig. 4A. For quantitative evaluation of the nonlinearity of these reservoir states, the reservoir outputs for normalized input voltages $V_n (= 0 \text{ to } -1)$ are shown in Fig. 4B, along with the input-output characteristics of a redox-IGR for comparison (*23*). The nonlinearity of the reservoir state $X(V_n)$ is quantified by the correlation coefficient $r_{\text{nonlinearity}}$ (Eq. 3) with the linear line ($Y_{\text{linear}} = -V_n$), where the correlation coefficient between $Y_{\text{linear}} = -V_n$ and reservoir state $X(V_n)$ is 1; the input-output characteristics of that reservoir state are perfectly linear. On the other

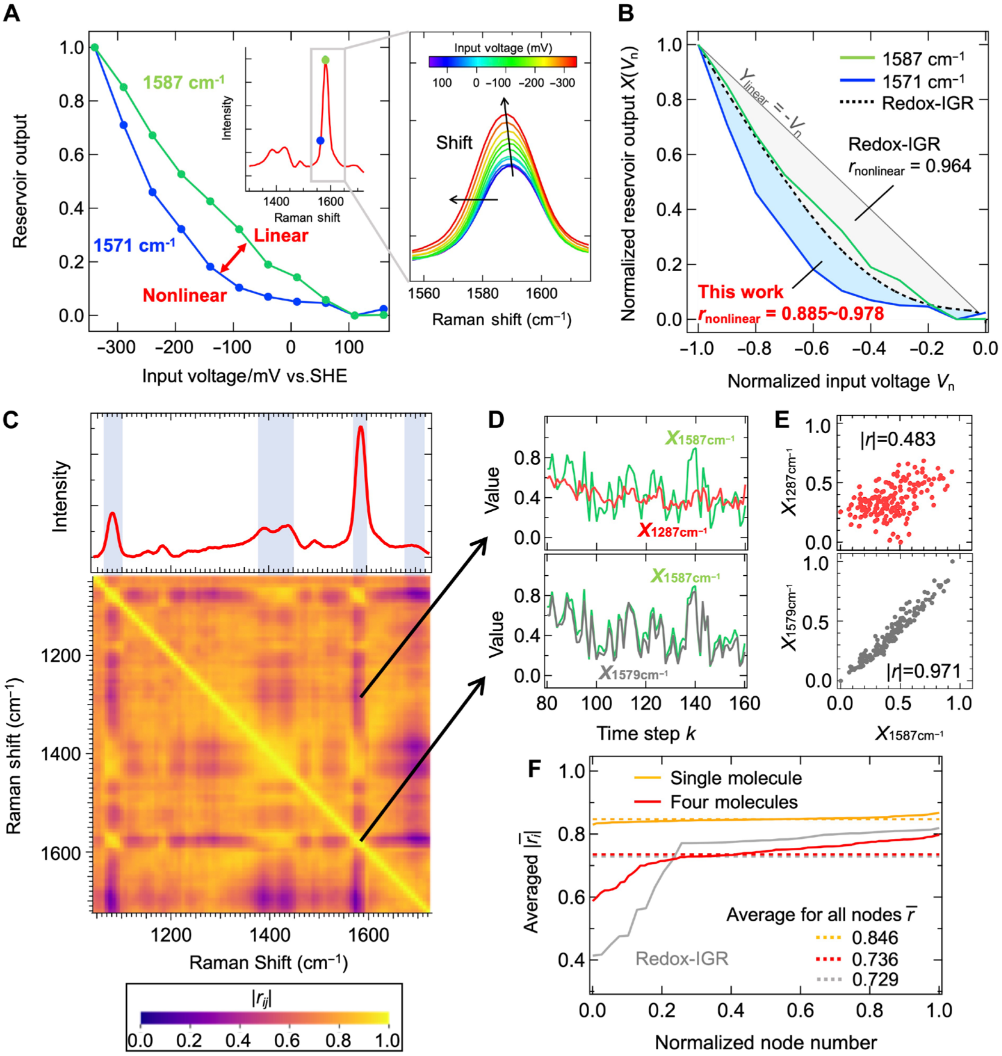

Fig. 4. Nonlinearity and high-dimensionality analysis. (**A**) Input voltage dependence of reservoir states obtained from 1571 cm^{-1} (blue line) and 1587 cm^{-1} (green line). (**B**) Comparison of nonlinearity with redox-IGR based on correlation coefficients. (**C**) Example of a Raman spectrum (top) and the correlation coefficients between reservoir states for random wave inputs obtained from the Raman spectrum (bottom). (**D**) Examples of reservoir states for combinations with relatively low correlation coefficients (top) and high correlation coefficients (bottom) (**E**) and their scatter plots. (**F**) Comparison of averaged correlation coefficients with redox-IGR for normalized node numbers. The dashed lines show averaged values for all nodes. The orange line shows the result of the single-molecule reservoir calculated from fig. S9.

hand, as $r_{\mathrm{nonlinearity}}$ gets closer to 0, the nonlinearity of the reservoir state becomes stronger

$$r_{\mathrm{nonlinearity}} = \frac{\sum\left[X(V_{\mathrm{n}})-\overline{X}\right]\left(Y_{\mathrm{linear}}-\overline{Y}_{\mathrm{linear}}\right)}{\sqrt{\sum\left[X(V_{\mathrm{n}})-\overline{X}\right]^{2}}\sqrt{\sum\left(Y_{\mathrm{linear}}-\overline{Y}_{\mathrm{linear}}\right)^{2}}} \quad (3)$$

where $\overline{X}$ is the average of X. The redox-IGR, which uses the redox reaction by ion gating to WO_3 as the nonlinear dynamics, has $r_{\mathrm{nonlinearity}} = 0.964$, which is close to 1 and the nonlinearity is weak. On the other hand, FM-RC, which uses the structural changes associated with local pH changes in the pMBA molecule as nonlinear dynamics, achieved a wide range of nonlinearities, from a strong nonlinearity ($r_{\mathrm{nonlinearity}} = 0.885$) in the reservoir state obtained at 1571 cm^{-1} to a weak nonlinearity ($r_{\mathrm{nonlinearity}}$ = 0.978) in the reservoir state obtained at 1587 cm^{-1} nonlinearity. Such coexistence of reservoir states with different nonlinearities has been reported to improve performance in full-simulation reservoirs such as the echo state network (ESN) (*63*) and in physical reservoirs such as IGRs (*22*–*24*). For example, an ESN with a mixture of linear and nonlinear nodes has shown improved scores in memory capacity and in the second-order nonlinear autoregressive moving average (NARMA2) task, which is similar to solving a second-order nonlinear dynamic equation task, compared to an ESN composed of only nonlinear nodes (*63*). It has also been reported that redox-IGR, which uses drain and gate currents based on different nonlinear dynamics, improves scores in memory capacity, solving a second-order nonlinear dynamic equation and NARMA2 tasks compared to the system that uses only drain currents (*23*). The excellent results in the nonlinear waveform transformation task are attributed to the good nonlinear characteristics of the FM-RC.

High dimensionality is, in addition to nonlinearity, another important property required of a reservoir. High dimensionality refers to the diversity of reservoir states, which is achieved by having many reservoir states that exhibit different behaviors from each other. In simulation reservoirs such as ESN, high dimensionality can be easily achieved simply by increasing the network size (number of nodes), and although the computational cost increases, memory capacity and computational performance also increase as the network size increases (*4*). On the other hand, in a physical reservoir, a sufficiently complex and diverse set of nodes based on the inherent nonlinear dynamics of the physical system is considered to inherently exist, but the number of effectively available nodes is not large due to the limited methods of accessing them (e.g., measurement probes). Therefore, to increase the number of nodes, the method usually adopted is that regarding the time evolution of reservoir states obtained from the physical system as spatially different nodes (virtual nodes) (*9–12*, *15*, *19–24*, *64*). However, as the number of virtual nodes increases, the number of similar nodes increases, thus limiting the higher dimensionality. Here, for the Raman spectra of detected structural changes of pMBA molecules in response to local pH changes, the intensities of different wave numbers were high-dimensionalized (without virtual nodes) as spatially distinct reservoir states. The correlation between reservoir state X_i and reservoir state X_j was quantified by the following correlation coefficient r_{ij}

$$r_{ij} = \frac{\sum_{k=1}^{L} \left[X_i(k) - \overline{X}_i\right]\left[X_j(k) - \overline{X}\right]}{\sqrt{\sum_{k=1}^{L} \left[X_i(k) - \overline{X}_i\right]^2}\sqrt{\sum_{k=1}^{L} \left[X_j(k) - \overline{X}_j\right]^2}} \tag{4}$$

The bottom panel of Fig. 4C shows the correlation coefficient $|r_{ij}|$ of the reservoir states of the subject FM-RC for random wave inputs. The darker areas in the figure indicate regions where the correlation coefficient is low and contributes to the high dimensionality of the reservoir, while the lighter areas in the figure indicate that the correlation coefficient is close to 1 and the reservoir states are similar to each other. To show how the reservoir states differ at these correlation coefficient values, the time evolution of the reservoir states is shown in Fig. 4D as an example of a combination with relatively low correlation coefficients ($X_{1587\mathrm{cm}^{-1}}$ and $X_{1287\mathrm{cm}^{-1}}$) and a combination with correlation coefficients close to 1 ($X_{1587\mathrm{cm}^{-1}}$ and $X_{1579\mathrm{cm}^{-1}}$). $X_{1587\mathrm{cm}^{-1}}$ and $X_{1287\mathrm{cm}^{-1}}$ shown in the top panel of Fig. 4D exhibit different behaviors from each other, whereas $X_{1587\mathrm{cm}^{-1}}$ and $X_{1579\mathrm{cm}^{-1}}$ shown in the bottom panel exhibit almost the same behavior. A scatter plot of these reservoir states is also shown in Fig. 4E. The $X_{1587\mathrm{cm}^{-1}}$ versus $X_{1287\mathrm{cm}^{-1}}$ plot shown in the top panel shows that the correlation coefficient between them corresponds to $|r_{ij}| = 0.483$, indicating that the correlation between them is relatively low, thus contributing to the high dimensionality of the reservoir. On the other hand, in the $X_{1587\mathrm{cm}^{-1}}$ versus $X_{1579\mathrm{cm}^{-1}}$ plot shown in the bottom panel of Fig. 4E, the correlation coefficient between them corresponds to $|r_{ij}| = 0.971$, which indicates that these reservoir states are almost completely correlated. In the $|r_{ij}|$ plot shown in the bottom panel of Fig. 4C, regions with particularly small correlation coefficients were identified in the reservoir states corresponding to certain wave number regions, and these correspond to the peak portions of the Raman spectra of the pMBA, as shown in the top panel of Fig. 4C. This indicates that the diversity of reservoir states in the subject FM-RC originates from the independent nonlinear behavior of the peaks, including minor structures, as shown in Fig. 4E. Figure S7 shows an example of the input-output characteristics (node nonlinearities) for each peak structure. Depending on the type of vibration mode, various Raman spectral nonlinear responses to the input voltage were observed. For example, the peak $X_{1581\mathrm{cm}^{-1}}$ corresponding to 1581 cm^{-1} responds relatively linearly to the input, whereas the peak $X_{1376\mathrm{cm}^{-1}}$ corresponding to 1376 cm^{-1} responds sharply above the threshold. Also, $X_{1226\mathrm{cm}^{-1}}$ responds quickly to relatively small input voltages, and $X_{1699\mathrm{cm}^{-1}}$ is a node that does not respond much to the input. (Such nodes serve as bias terms in reservoir calculations.) Because of the inclusion of these various nonlinear functions f in the system, based on the vibrational dynamics of the molecules, our system has achieved high dimensionality even though it consists of only one to four molecules. Figure S8 shows a schematic of the higher dimensionality method in our system. The input one-dimensional time series data $u(k)$ is converted to Raman spectra by the molecular reservoir system. These Raman spectra can be regarded as spatially distinct nodes with respect to the wave number direction. At each wave number, the system output can map the input time series data to a higher dimensional reservoir state space because the nonlinear mapping is based on different nonlinear functions as shown in figs. S7 and S8. Figure S9 shows a heat map of the correlation coefficients obtained from the Raman spectra of a pMBA single molecule. Compared to the heatmap of a few molecules shown in Fig. 4C, the high dimensionality of the single molecule is lower because there are clearly fewer minor peak structures observed in the single pMBA molecule. The average correlation coefficient $\overline{r}_i$ (Eq. 5) for a given node i, sorted in decreasing order and plotted by normalized node number, is shown in Fig. 4F

$$\overline{r}_i = \frac{1}{N-1}\sum_{j \neq i}^{N} r_{ij} \tag{5}$$

The redox-IGR results are also shown as a comparison (*23*), with the average value $\overline{r} = \sum_{i=1}^{N} \overline{r}_i / N$ for all nodes, indicated by the dotted line. The all-node average correlation coefficients for both are almost identical, indicating that the subject FM-RC has the same high dimensionality as a redox-IGR with virtual nodes, even though it does not use virtual nodes. $\overline{r}_i$ of the FM-RC is particularly small in the region where the normalized node number is below 0.2 (that is, 20% of all reservoir states). These reservoir states correspond to the peaks of the Raman spectra. Although this study focuses on the computational power realized by only a few pMBA molecules, the coexistence of molecules that peak at different wave numbers from pMBA, for example, has the potential to markedly increase the overall high dimensionality.

From these results, it can be concluded that the high computational performance of the subject FM-RC is based on good nonlinear characteristics, as shown in Fig. 4 (A and B), in addition to a sufficiently high dimensionality that is comparable to that of redox-IGR. Thus, it outperforms other physical reservoirs in the nonlinear waveform transformation task, where the nonlinearities outlined in Fig. 2 are particularly required for the reservoir. This is an extraordinary outcome for a result realized from only a few molecules. Furthermore, such nonlinearity and high dimensionality can be markedly enhanced by using molecules that respond differently to ion gating in a composite manner, so the results of this study expand the possibilities of molecular computing and provide the potential for realizing efficient information processing systems based on the local pH response dynamics of molecules.

Blood glucose level prediction task

Last, we performed the prediction of blood glucose levels task by FM-RC as a more difficult and practical task. As discussed in Figs. 2 and 3, the operating speed of FM-RC is as slow as 10 seconds per input event (0.1 Hz). However, PRC based on these slow dynamics is an advantageous feature for direct information processing of slow time series signals such as blood glucose levels. Time-series data of blood glucose levels used for the task were measured at 5-min intervals in patients with type 1 diabetes provided by the Diabetes Research in Children Network (DirecNet) as shown in fig. S10 (*65*). Details of the method and learning algorithm are given in Materials and Methods.

Figure 5A shows the target waveform and the FM-RC prediction waveform for the one-step-ahead prediction (i.e., 5-min-ahead prediction) task. The FM-RC prediction waveform captures the trend of the signal very well, although it is not a perfect match with the target waveform, indicating that FM-RC can predict blood glucose levels. Figure 5B shows the predicted length dependence of the RMSE. Compared to the CNT-based reservoir (*39*), shown in the gray plot, the prediction error of FM-RC is notably small, e.g., RMSE = 25.0 mg/dl for FM-RC compared to RMSE = 47.0 mg/dl for the CNT-based reservoir in the 15-min-ahead prediction task. It was also reported that the full-simulation recurrent neural network achieved RMSE = 18.9 mg/dl in the 30-min-ahead prediction task, and FM-RC could not come close to this performance (*66*). However, this task is challenging and, to our knowledge, has only been experimentally demonstrated on physical reservoirs in this study and the CNT-based reservoirs, and our FM-RC achieved a 47% lower error than the previous studies (*39*). Therefore, these results demonstrate the high computational performance of FM-RC and its potential application to time series data processing based on slow dynamics.

DISCUSSION

Few- and single-molecule RC was firstly demonstrated on the basis of the molecular vibration dynamics of pMBA in WO_x@Ag-NPs systems, measured by means of SERS. The Raman signal of the few pMBA molecules, absorbed at the SERS active site of WO_x@Ag-NPs, were successfully detected under various local pH conditions, which were attained by applied ion-gating stimuli corresponding to input signals in RC. The reversible nonlinear response of pMBA SERS spectra was used for performing RC on pattern recognition and prediction tasks. In nonlinear waveform transformation tasks, the subject system achieved 95.1 to 97.7% accuracy with respect to various waveforms and phase shifts, which accuracy is better than the scores reported for atomic switch NWN reservoirs and a solid electrolyte/diamond–based EDL-IGR (*8*, *16*, *18*, *24*). In solving a second-order nonlinear dynamic equation task, the system achieved 94.3% accuracy, which is comparable to other physical reservoirs reported to date (*5*, *11*, *22*, *23*). Furthermore, our molecule reservoir achieved good prediction performance in the 15-min-ahead prediction task for blood glucose levels, with RMSE of 25.0 mg/dl for four pMBA molecules and 42.1 mg/dl for a single pMBA molecule. This is a 47% smaller prediction error than the previously reported physical reservoir (*39*). Molecular computing has long been a goal in the study of nanoelectronics, as it is expected to enable extremely high integration due to the small volume of molecules it uses (*47*–*49*, *67*). Since FM-RC is an effective approach to maximizing the value of the inherent properties (information) of molecules by applying the spatiotemporal dynamics of molecules directly to computations, it can be viewed as an emerging building block of the next generation of molecular computing–based AI systems, not only in conventional logic circuits for von Neumann computing but also as RC circuits in unconventional computing (*2*, *3*). Such next-generation AI systems are promising for implementation in edge AI computing, which performs efficient information processing integrated with sensing. Since FM-RC consists of optical systems for SERS measurement and a solution cell, it is preferred to be implemented in industrial facilities where these setups are acceptable. For example, the FM-RC is expected to be incorporated into manufacturing facilities in factories and connected to sensors such as cameras and microphones to detect abnormalities in manufacturing lines (work condition estimation using sound and image data), visualize work processes (identification of work contents using image data), and control robot arms (estimation of dynamics using motion sensors). In addition, the optimization of a charge-coupled device (CCD) that

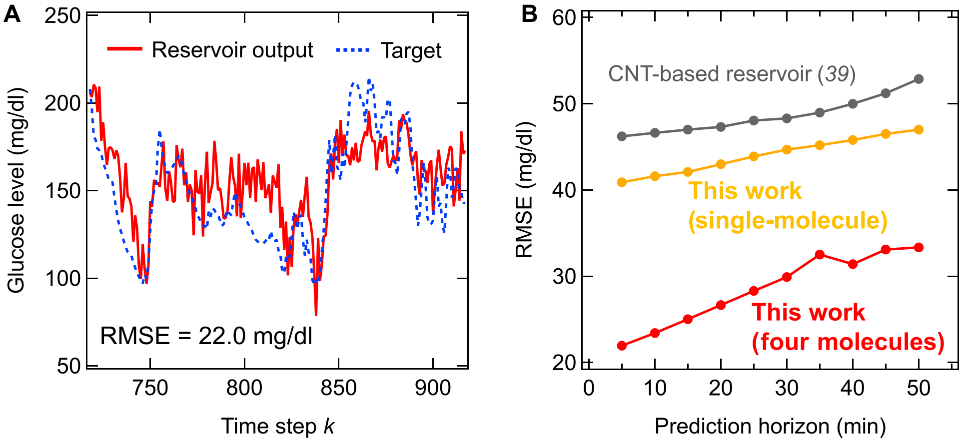

Fig. 5. Blood glucose level prediction task. (**A**) Target and prediction waveforms of one-step-ahead prediction task at the test phase. (**B**) Prediction error as a function of the prediction horizon. Gray plots show the results of the CNT-based reservoir as a comparison (*39*).

measures SERS signals is expected to improve the integration of FM-RC with the computing infrastructure that performs information processing in readout networks (linear classifiers). Since it is not necessary to acquire the entire SERS signal for edge AI computing applications, only the signal intensities of specific wave number components used for information processing need to be detected with high accuracy, and the detected signal (reservoir state) can be digitally converted and transmitted to the existing computing infrastructure to perform learning/classification in the readout network. Furthermore, if the detected reservoir states are directly input as analog signals to the linear classifier consisting of an array of variable resistor elements such as memristors (*68*, *69*), and only the analysis results are transferred to the computing infrastructure, then further reductions in computational resources, power consumption, and communication costs can be expected. FM-RC is particularly suited to be combined with electrochemical processes (*70*–*74*) or nanoarchitectonic materials (*75*–*79*) so as to enhance complexity as a dynamical system. Explorations are underway to identify the optimal molecules and detection systems that are most suitable for high-performance molecular RC.

MATERIALS AND METHODS

Fabrication and measurement of the few-molecule RC

The WO_x nanorods used as SERS active nanomaterials were prepared in an ultrahigh vacuum chamber at an atmosphere of 8×10^{-4} Pa O_2, by sublimation of tungsten oxide from a tungsten filament. This was then heated to 1100°C and placed 20 mm in front of a 0.2-mm-diameter tungsten wire, which was heated to 700° to 800°C (*52*–*54*). The typical growth time was 10 hours. Numerous WO_x nanorods, with diameters of 20 to 100 nm and lengths of 1 to 10 μm, were grown on the tungsten wire. One such nanorod was selected and fixed to the apex of the tungsten tip sharpened by electrochemical etching. The WO_x nanorod was fine-tuned in position using a piezo-controlled stage and fixed using epoxy resin while being observed under an optical microscope in the air.

SERS measurements were performed using a micro-Raman system (HORIBA Jobin-Yvon, HR-800). The measurements were performed in 0.15 M NaCl aqueous solution. A 488-nm wavelength laser beam was focused, with a spot diameter of 500 nm, on the WO_x nanorod at the apex of a tungsten tip using a 100× water immersion objective lens. The backscattered light was collected by the said objective and introduced into the spectrometer, after removing Rayleigh light with an edge filter, and was detected by a liquid nitrogen–cooled CCD. The electrode potential was controlled by a potentiostat in a three-electrode configuration. A tungsten wire with a WO_x nanorod attached to its apex was used as the working electrode, and platinum wires were used as the counter electrode and pseudo-reference electrode.

The subject WO_x nanorod was modified with silver nanoparticles in the same configuration as the SERS measurements. Ten nanomolars of $AgNO_3$ and 6 μM polydopamine in 0.15 M NaCl solution were used. Polydopamine was added to confirm from the Raman spectra that the SERS active sites were formed by Ag electrodeposition. WO_x nanorods were irradiated with 488-nm laser light at 2-mW intensity, while −340 to −840 mV versus SHE was applied to form silver nanoparticles, by electrodeposition of silver, at the light-irradiated position. The tungsten tip, with silver-modified WO_x nanorod, was removed from the aqueous solution and transferred to a 10 μM pMBA in 0.15 M NaCl aqueous solution for RC.

The SEM image of the silver-modified WO_x nanorod is shown in fig. S1. The nanorod was fixed to a tungsten tip using epoxy resin, but the tip edge was not covered with epoxy resin, so the WO_x nanorod and the tungsten tip were electrically contacted. Hence, silver nanoparticles could be formed on the nanorods by electrodeposition as shown in Fig. 1C. Therefore, the voltage signal applied to the working electrode was surely applied to the WO_x nanorod.

The silver-modified WO_x nanorod was observed with TEM and energy-dispersive x-ray spectroscopy (EDS) (JEOL, JEM-ARM200F). For TEM observation, a tungsten tip with a silver-modified WO_x nanorod attached at the apex was cut into a 1-mm-long piece and fixed to a TEM grid using silver epoxy.

Nonlinear waveform transformation task

The following explains the method used to perform the waveform transformation task that was demonstrated to evaluate the nonlinear transformation capability of the subject molecule reservoir. In the waveform transformation task, a triangular wave was used as input, and the target waveforms $T(k)$ were sin wave (Sin), square wave (Square), π/2 phase-shifted triangular wave (Shift), and frequency-doubled triangular wave (2f). The input triangular wave (fig. S4A) was converted to a step-like voltage signal (10 seconds per step, 20 steps per period) and input to the molecule reservoir. The applied voltage ranged from +160 to −340 mV versus SHE and the frequency of the triangular wave was 5 mHz, as shown in fig. S4B. Fourteen periods of triangular waveforms were input to the molecule reservoir, and 10 periods were used for computing, excluding the first 4 periods to make the reservoir steady state. SERS measurements were made by integrating for 10 s corresponding to each voltage step, and the obtained Raman spectra were smoothed by moving average. From the Raman spectra in the region from 945 to 1728 cm^{-1}, which contains several peaks, the signal intensity every 3.92 cm^{-1} was taken as the reservoir state. Therefore, the total reservoir size (the number of reservoir states) N was 200. These reservoir states were manually obtained from the Raman spectra and input directly into the readout network (a linear classifier with 200 nodes in the input layer and one node in the output layer). The reservoir output $y(k)$ is the linear sum of the readout weight vector $\boldsymbol{W}$ and the reservoir state vector $\boldsymbol{x}(k)$ at a certain time step k, as shown in Eq. 1. The weight matrix $\boldsymbol{W}$ was learned by ridge regression, so that the reservoir output matches the target waveform $T(k)$. The cost function J in the ridge regression is defined by following Eq. 6

$$J(W) = \frac{1}{2}\sum_{k=1}^{L}\left[T(k) - Y(k)\right]^2 + \frac{\lambda}{2}\sum_{i=1}^{N} w_i^2 \tag{6}$$

where L (=200) and λ (=10^{-6}) are the data length and regularization parameters, respectively. The trained weight vector $\boldsymbol{W}$ that minimizes J is given by following Eq. 7

$$\boldsymbol{W} = \boldsymbol{T}\boldsymbol{X}^{\mathrm{T}}(\boldsymbol{X}\boldsymbol{X}^{\mathrm{T}} + \lambda\boldsymbol{I})^{-1} \tag{7}$$

where $\boldsymbol{T} = [\boldsymbol{T}(1), \boldsymbol{T}(2), \ldots, \boldsymbol{T}(L)]$, $\boldsymbol{X} = [\boldsymbol{X}(1), \boldsymbol{X}(2), \ldots, \boldsymbol{x}(L)]$, and $\boldsymbol{I}(\subseteq \mathbb{R}^{N\times N})$ are the target output matrix, the reservoir state matrix, and the identify matrix, respectively. The readout network and weights were stored and operated on a personal computer. It would be possible to physically implement a readout network by installing an array of programmable analog resistance-changing devices (artificial synaptic devices) such as memristors and redox transistors (*68*, *69*). For training the readout weights, we used the supervised data $T(k)$, shown in fig. S3. For all transformation tasks, the number of samples (data length) in the training dataset was 200 (10 periods×20 steps). The computational performance of the reservoir was evaluated by the accuracy (Eq. 8) calculated from the normalized mean square error (NMSE) between the reservoir output and the target (*8*, *16*, *18*, *24*)

$$\text{Accuracy} = 1 - \sqrt{\text{NMSE}} \tag{8}$$

$$\text{NMSE} = \frac{\sum_{k=1}^{L}\left[T(k) - y(k)\right]^2}{\sum_{k=1}^{L} T^2(k)} \tag{9}$$

We also calculated the mean square error (MSE) given by the following Eq.10, which is a general error indicator

$$\text{MSE} = \frac{1}{L}\sum_{k=1}^{L}\left[T(k) - y(k)\right]^2 \tag{10}$$

Note that comparisons of MSE between different time-series data are not meaningful because the characteristics of the target data are not taken into account in MSE.

Solving a second-order nonlinear dynamic equation task

In the second-order nonlinear equation task, a random input $u(k)$ (fig. S6A) was converted to a step-like voltage signal from +160 to −340 mV versus SHE (fig. S6B) and input to the device. As in the waveform conversion task, one step was 10 s (0.1 Hz), and the Raman spectra were measured by integrating for 10 s, corresponding to each voltage step. The input random wave was 255 steps. To avoid the influence of noise and to verify the computational capability of the molecule reservoir, the input was applied six times and the average of the Raman spectra obtained was smoothed by a moving average. From the Raman spectra in a region of from 1041 cm^{-1} to 1726 cm^{-1}, which contains several peaks, the signal intensity every 7.87 cm^{-1} was taken as the reservoir state. Therefore, the total reservoir size (the number of reservoir states) N was 88. To prevent overlearning in this task, N was set smaller than in the nonlinear waveform transformation task. These reservoir states were manually taken from the Raman spectrum and normalized from 0 to 1, then input into a readout network (a linear classifier with 88 nodes in the input layer and one node in the output layer). The readout weights were trained by ridge regression as in the waveform transformation task. However, the ridge parameter λ was 1.0 and the data length L was 160 for the training phase and 95 for the testing phase. Figure S6 shows the dataset used in this task. The input random wave $u(k)$ is a random sequence ranging from 0 to 0.5, based on a uniform distribution. The target waveform was obtained by substituting this random wave into Eq. 2. For training the readout weights, a training dataset with 160 samples (data length L) was used, as shown in fig. S6C. For testing, we used the test dataset with 95 samples (data length L), shown in fig. S6C. In ridge regression, the weights that minimize the cost function shown in Eq. 6 are uniquely determined by Eq. 7. Therefore, multiple training epochs are not required in training, such as the gradient descent method generally used in the training of neural networks. Computational performance was evaluated by the accuracy shown in Eq. 8. In a previous study (*5*, *11*, *21*, *22*), to which we compared the results as shown in Fig. 3D, the computational performance was reported by NMSE as shown in Eq. 9, so this was converted to the accuracy in Eq. 8 and subsequently presented.

In the second-order nonlinear equation task shown in Fig. 3, the task was performed by obtaining 88 reservoir states from Raman spectra for equally spaced predefined wave numbers, as described above. This method does not require peak detection and thus reduces the additional computational cost of analyzing the SERS signal, as well as the hyperparameters for the conditions for obtaining the reservoir states. The prediction accuracy of the second-order nonlinear equation task using this method was comparable to that of the case where only the peak portion is selectively used as the reservoir state ($N = 88$), as shown in fig. S12. Therefore, this method is suitable for applying this system to edge computing in a simple method. Please refer to section S2 for more details on the results of the tasks performed using the peak portion as the reservoir state selectively.

Blood glucose level prediction task

Time-series data of blood glucose levels provided by DirecNet (Diabetes Research in Children Network) (*65*) were used for the input signal $u(k)$, which was converted into a step-like voltage signal from +160 to −340 mV versus SHE in 5 seconds per step. The Raman spectra were measured by integrating for 5 s, corresponding to each voltage step. To avoid the influence of noise and to verify the computational capability of the molecule reservoir, the input was applied three times and the average of the Raman spectra obtained was smoothed by a moving average. From the Raman spectra in a region of from 1041 to 1726 cm^{-1}, the signal intensity every 7.87 cm^{-1} was taken as the reservoir state. Therefore, the total reservoir size (the number of reservoir states) N was 88. These reservoir states were manually obtained from the Raman spectra and input directly into the readout network (a linear classifier with 88 nodes in the input layer and one node in the output layer). Figure S10 shows the dataset used in this task. The target waveform $T(k)$ was obtained by $T(k) = u(k + n)$ for the n-step-ahead prediction task. The first 17 steps were used for washing out the reservoir. For training the readout weights, a training dataset with 700 samples (data length L) was used. For testing, we used the test dataset with 200 samples (data length L). The readout weights were trained by ridge regression as in the waveform transformation task. However, the ridge parameter λ was 100 and the data length L was 700 for the training phase and 200 for the testing phase. Computational performance was evaluated by the RMSE shown in Eq. 11

$$\text{RMSE} = \sqrt{\frac{1}{L}\sum_{k=1}^{L}\left[T(k) - y(k)\right]^2} \tag{11}$$

Supplementary Materials

This PDF file includes:

Sections S1 and S2
Figs. S1 to S12
Table S1

REFERENCES AND NOTES

1. Y. LeCun, Y. Bengio, G. Hinton, Deep learning. *Nature* **521**, 436–444 (2015).
2. G. Tanaka, T. Yamane, J. B. Héroux, R. Nakane, N. Kanazawa, S. Takeda, H. Numata, D. Nakano, A. Hirose, Recent advances in physical reservoir computing: A review. *Neural Netw.* **115**, 100–123 (2019).
3. K. Nakajima, Physical reservoir computing—An introductory perspective. *Jpn. J. Appl. Phys.* **59**, 060501 (2020).

4. H. Jaeger, H. Haas, Harnessing nonlinearity: Predicting chaotic systems and saving energy in wireless communication. *Science* **304**, 78–80 (2004).
5. C. Du, F. Cai, M. A. Zidan, W. Ma, S. H. Lee, W. D. Lu, Reservoir computing using dynamic memristors for temporal information processing. *Nat. Commun.* **8**, 2204 (2017).
6. J. Moon, W. Ma, J. H. Shin, F. Cai, C. Du, S. H. Lee, W. D. Lu, Temporal data classification and forecasting using a memristor-based reservoir computing system. *Nat. Electron.* **2**, 480–487 (2019).
7. R. Midya, Z. Wang, S. Asapu, X. Zhang, M. Rao, W. Song, Y. Zhuo, N. Upadhyay, J. J. Yang, Reservoir computing using diffusive memristors. *Adv. Intell. Syst.* **1**, 1900084 (2019).
8. K. Fu, R. Zhu, A. Loeffler, J. Hochstetter, A. Diaz-Alvarez, A. Stieg, J. Gimzewski, T. Nakayama, Z. Kuncic, Reservoir computing with neuromemristive nanowire networks, in *2020 International Joint Conference on Neural Networks (IJCNN)* (IEEE, 2020), pp. 1–8.
9. Y. Zhong, J. Tang, X. Li, B. Gao, H. Qian, H. Wu, Dynamic memristor-based reservoir computing for high-efficiency temporal signal processing. *Nat. Commun.* **12**, 408 (2021).
10. J. Torrejon, M. Riou, F. A. Araujo, S. Tsunegi, G. Khalsa, D. Querlioz, P. Bortolotti, V. Cros, K. Yakushiji, A. Fukushima, H. Kubota, S. Yuasa, M. D. Stiles, J. Grollier, Neuromorphic computing with nanoscale spintronic oscillators. *Nature* **547**, 428–431 (2017).
11. W. Jiang, L. Chen, K. Zhou, L. Li, Q. Fu, Y. Du, R. H. Liu, Physical reservoir computing using magnetic skyrmion memristor and spin torque nano-oscillator. *Appl. Phys. Lett.* **115**, 192403 (2019).
12. W. Namiki, D. Nishioka, Y. Yamaguchi, T. Tsuchiya, T. Higuchi, K. Terabe, Experimental demonstration of high-performance physical reservoir computing with nonlinear interfered spin wave multidetection. *Adv. Intell. Syst.* **5**, 2300228 (2023).
13. K. Nakajima, H. Hauser, T. Li, R. Pfeifer, Information processing via physical soft body. *Sci. Rep.* **5**, 10487 (2015).
14. H. O. Sillin, R. Aguilera, H. H. Shieh, A. V. Avizienis, M. Aono, A. Z. Stieg, J. K. Gimzewski, A theoretical and experimental study of neuromorphic atomic switch networks for reservoir computing. *Nanotechnology* **24**, 384004 (2013).
15. X. Zhu, Q. Wang, W. D. Lu, Memristor networks for real-time neural activity analysis. *Nat. Commun.* **11**, 2439 (2020).
16. J. Hochstetter, R. Zhu, A. Loeffler, A. Diaz-Alvarez, T. Nakayama, Z. Kuncic, Avalanches and edge-of-chaos learning in neuromorphic nanowire networks. *Nat. Commun.* **12**, 4008 (2021).
17. G. Milano, G. Pedretti, K. Montano, S. Ricci, S. Hashemkhani, L. Boarino, D. Ielmini, C. Ricciardi, In materia reservoir computing with a fully memristive architecture based on self-organizing nanowire networks. *Nat. Mater.* **21**, 195–202 (2022).
18. E. C. Demis, R. Aguilera, K. Scharnhorst, M. Aono, A. Z. Stieg, J. K. Gimzewski, Nanoarchitectonic atomic switch networks for unconventional computing. *Jpn. J. Appl. Phys.* **55**, 1102B2 (2016).
19. M. Nakajima, K. Inoue, K. Tanaka, Y. Kuniyoshi, T. Hashimoto, K. Nakajima, Physical deep learning with biologically inspired training method: Gradient-free approach for physical hardware. *Nat. Commun.* **13**, 7847 (2022).
20. Y. Paquot, F. Duport, A. Smerieri, J. Dambre, B. Schrauwen, M. Haelterman, S. Massar, Optoelectronic reservoir computing. *Sci. Rep.* **2**, 287 (2012).
21. G. Van der Sande, D. Brunner, M. C. Soriano, Advances in photonic reservoir computing. *Nanophotonics* **6**, 561–576 (2017).
22. D. Nishioka, T. Tsuchiya, W. Namiki, M. Takayanagi, M. Imura, Y. Koide, T. Higuchi, K. Terabe, Edge-of-chaos learning achieved by ion-electron–coupled dynamics in an ion-gating reservoir. *Sci. Adv.* **8**, eade1156 (2022).
23. T. Wada, D. Nishioka, W. Namiki, T. Tsuchiya, T. Higuchi, K. Terabe, A redox-based ion-gating reservoir, utilizing double reservoir states in drain and gate nonlinear responses. *Adv. Intell. Syst.* **5**, 2300123 (2023).
24. M. Takayanagi, D. Nishioka, T. Tsuchiya, M. Imura, Y. Koide, T. Higuchi, K. Terabe, Ultrafast-switching of an all-solid-state electric double layer transistor with a porous yttria-stabilized zirconia proton conductor and the application to neuromorphic computing. *Mater. Today Adv.* **18**, 100393 (2023).
25. M. Akai-Kasaya, Y. Takeshima, S. Kan, K. Nakajima, T. Oya, T. Asai, Performance of reservoir computing in a random network of single-walled carbon nanotubes complexed with polyoxometalate. *Neuromorph. Comput. Eng.* **2**, 014003 (2022).
26. H. Tanaka, M. Akai-Kasaya, A. TermehYousefi, L. Hong, L. Fu, H. Tamukoh, D. Tanaka, T. Asai, T. Ogawa, A molecular neuromorphic network device consisting of single-walled carbon nanotubes complexed with polyoxometalate. *Nat. Commun.* **9**, 2693 (2018).
27. M. Cucchi, H. Kleemann, H. Tseng, G. Ciccone, A. Lee, D. Pohl, K. Leo, Directed growth of dendritic polymer networks for organic electrochemical transistors and artificial synapses. *Adv. Electron. Mater.* **7**, 2100586 (2021).
28. M. Cucchi, C. Gruener, L. Petrauskas, P. Steiner, H. Tseng, A. Fischer, B. Penkovsky, C. Matthus, P. Birkholz, H. Kleemann, K. Leo, Reservoir computing with biocompatible organic electrochemical networks for brain-inspired biosignal classification. *Sci. Adv.* **7**, eabh0693 (2021).
29. Y. Usami, B. van de Ven, D. G. Mathew, T. Chen, T. Kotooka, Y. Kawashima, Y. Tanaka, Y. Otsuka, H. Ohoyama, H. Tamukoh, H. Tanaka, W. G. van der Wiel, T. Matsumoto, In-materio reservoir computing in a sulfonated polyaniline network. *Adv. Mater.* **33**, e2102688 (2021).
30. X. Wu, S. Wang, W. Huang, Y. Dong, Z. Wang, W. Huang, Wearable in-sensor reservoir computing using optoelectronic polymers with through-space charge-transport characteristics for multi-task learning. *Nat. Commun.* **14**, 468 (2023).
31. S. G. Koh, H. Shima, Y. Naitoh, H. Akinaga, K. Kinoshita, Reservoir computing with dielectric relaxation at an electrode–ionic liquid interface. *Sci. Rep.* **12**, 6958 (2022).
32. T. Matsuo, D. Sato, S. G. Koh, H. Shima, Y. Naitoh, H. Akinaga, T. Itoh, T. Nokami, M. Kobayashi, K. Kinoshita, Dynamic nonlinear behavior of ionic liquid-based reservoir computing devices. *ACS Appl. Mater. Interfaces* **14**, 36890–36901 (2022).
33. S. Kan, K. Nakajima, T. Asai, M. Akai-Kasaya, Physical implementation of reservoir computing through electrochemical reaction. *Adv. Sci.* **9**, 2104076 (2022).
34. W. Yahiro, N. Aubert-Kato, M. Hagiya A reservoir computing approach for molecular computing, in *ALIFE 2018: The 2018 Conference on Artificial Life* (MIT Press, 2018), pp. 31–38.
35. B. Jones, D. Stekel, J. Rowe, C. Fernando Is there a liquid state machine in the bacterium escherichia coli? in *2007 IEEE Symposium on Artificial Life* (IEEE, 2007), pp. 187–191.
36. A. Goudarzi, M. R. Lakin, D. Stefanovic DNA Reservoir Computing: A novel molecular computing approach, in *DNA Computing and Molecular Programming*, D. Soloveichik, B. Yurke, Eds. (Springer International Publishing, 2013), pp. 76–89.
37. N. Lobato-Dauzier, L. Cazenille, T. Fujii, A. Genot, N. Aubert-Kato temperature-based inputs for molecular reservoir computers, in *Artificial Life Conference Proceedings 32* (MIT Press, 2020), pp. 420–422.
38. M. R. Hossain, A. S. Mohamed, N. X. Armendarez, J. S. Najem, M. S. Hasan, Biomembrane-based memcapacitive reservoir computing system for energy-efficient temporal data processing. *Adv. Intell. Syst.* **5**, 2300346 (2023).
39. T. Shingu, H. Uchiyama, T. Watanabe, Y. Ohno, Electrochemical reservoir computing based on surface-functionalized carbon nanotubes. *Carbon* **214**, 118344 (2023).
40. Y. Shingaya, H. Takaki, N. Kobayashi, M. Aono, T. Nakayama, Single-molecule detection with enhanced Raman scattering of tungsten oxide nanostructure. *Nanoscale* **14**, 14552–14557 (2022).
41. L. Zhao, Y. Shingaya, H. Tomimoto, Q. Huang, T. Nakayama, Functionalized carbon nanotubes for pH sensors based on SERS. *J. Mater. Chem.* **18**, 4759–4761 (2008).
42. L. Zhang, Q. Zhao, Z. Jiang, J. Shen, W. Wu, X. Liu, Q. Fan, W. Huang, Recent progress of SERS nanoprobe for pH detecting and its application in biological imaging. *Biosensors* **11**, 282 (2021).
43. A. Michota, J. Bukowska, Surface-enhanced Raman scattering (SERS) of 4-mercaptobenzoic acid on silver and gold substrates. *J. Raman Spectrosc.* **34**, 21–25 (2003).
44. A. Kudelski, Surface-enhanced Raman scattering study of monolayers formed from mixtures of 4-mercaptobenzoic acid and various aromatic mercapto-derivative bases. *J. Raman Spectrosc.* **40**, 2037–2043 (2009).
45. C. E. Talley, L. Jusinski, C. W. Hollars, S. M. Lane, T. Huser, Intracellular pH sensors based on surface-enhanced Raman scattering. *Anal. Chem.* **76**, 7064–7068 (2004).
46. L. M. Adleman, Molecular computation of solutions to combinatorial problems. *Science* **266**, 1021–1024 (1994).
47. T. Rueckes, K. Kim, E. Joselevich, G. Y. Tseng, C. L. Cheung, C. M. Lieber, Carbon nanotube-based nonvolatile random access memory for molecular computing. *Science* **289**, 94–97 (2000).
48. J. M. Tour, Molecular electronics. Synthesis and testing of components. *Acc. Chem. Res.* **33**, 791–804 (2000).
49. C. P. Collier, E. W. Wong, M. Belohradský, F. M. Raymo, J. F. Stoddart, P. J. Kuekes, R. S. Williams, J. R. Heath, Electronically configurable molecular-based logic gates. *Science* **285**, 391–394 (1999).
50. G. Paun, G. Rozenberg, A. Salomaa, *DNA Computing: New Computing Paradigms* (Springer Science & Business Media, 2005).
51. Y. Benenson, B. Gil, U. Ben-Dor, R. Adar, E. Shapiro, An autonomous molecular computer for logical control of gene expression. *Nature* **429**, 423–429 (2004).
52. Y. Shingaya, T. Nakayama, M. Aono, Epitaxial growth of WO_x nanorod array on W(001). *Sci. Technol. Adv. Mater.* **5**, 647–649 (2004).
53. O. Kubo, Y. Shingaya, M. Nakaya, M. Aono, T. Nakayama, Epitaxially grown WO_x nanorod probes for sub-100nm multiple-scanning-probe measurement. *Appl. Phys. Lett.* **88**, 254101–254103 (2006).
54. T. Nakayama, O. Kubo, Y. Shingaya, S. Higuchi, T. Hasegawa, C.-S. Jiang, T. Okuda, Y. Kuwahara, K. Takami, M. Aono, Development and application of multiple-probe scanning probe microscopes. *Adv. Mater.* **24**, 1675–1692 (2012).
55. R. Li, H. Lv, X. Zhang, P. Liu, L. Chen, J. Cheng, B. Zhao, Vibrational spectroscopy and density functional theory study of 4-mercaptobenzoic acid. *Spectrochim. Acta A Mol. Biomol. Spectrosc.* **148**, 369–374 (2015).
56. Y. Liu, H. Yuan, A. M. Fales, T. Vo-Dinh, PH-sensing nanostar probe using surface-enhanced Raman scattering (SERS): Theoretical and experimental studies. *J. Raman Spectrosc.* **44**, 980–986 (2013).

57. A. M. Gardner, T. G. Wright, Consistent assignment of the vibrations of monosubstituted benzenes. *J. Chem. Phys.* **135**, 114305 (2011).
58. S. M. Stranahan, K. A. Willets, Super-resolution optical imaging of single-molecule SERS hot spots. *Nano Lett.* **10**, 3777–3784 (2010).
59. J. A. Dieringer, R. B. Lettan II, K. A. Scheidt, R. P. Van Duyne, A frequency domain existence proof of single-molecule surface-enhanced Raman spectroscopy. *J. Am. Chem. Soc.* **129**, 16249–16256 (2007).
60. Y. Sharaabi, T. Shegai, G. Haran, Two-state analysis of single-molecule Raman spectra of crystal violet. *Chem. Phys.* **318**, 44–49 (2005).
61. N. Bertschinger, T. Natschläger, Real-time computation at the edge of chaos in recurrent neural networks. *Neural Comput.* **16**, 1413–1436 (2004).
62. C. G. Langton, Computation at the edge of chaos: Phase transitions and emergent computation. *Phys. D: Nonlinear Phenom.* **42**, 12–37 (1990).
63. M. Inubushi, K. Yoshimura, Reservoir computing beyond memory-nonlinearity trade-off. *Sci. Rep.* **7**, 10199 (2017).
64. L. Appeltant, M. C. Soriano, G. Van der Sande, J. Danckaert, S. Massar, J. Dambre, B. Schrauwen, C. R. Mirasso, I. Fischer, Information processing using a single dynamical node as complex system. *Nat. Commun.* **2**, 468 (2011).
65. Diabetes Research in Children Network (DIRECNET) Study Group, The accuracy of the CGMS™ in children with type 1 diabetes: Results of the diabetes research in children network (DirecNet) accuracy study. *Diabetes Technol. Ther.* **5**, 781–789 (2003).
66. J. Martinsson, A. Schliep, B. Eliasson, O. Mogren, Blood glucose prediction with variance estimation using recurrent neural networks. *J. Healthc. Inform. Res.* **4**, 1–18 (2020).
67. C. Joachim, J. K. Gimzewski, A. Aviram, Electronics using hybrid-molecular and mono-molecular devices. *Nature* **408**, 541–548 (2000).
68. M. Rao, H. Tang, J. Wu, W. Song, M. Zhang, W. Yin, Y. Zhuo, F. Kiani, B. Chen, X. Jiang, H. Liu, H.-Y. Chen, R. Midya, F. Ye, H. Jiang, Z. Wang, M. Wu, M. Hu, H. Wang, Q. Xia, N. Ge, J. Li, J. J. Yang, Thousands of conductance levels in memristors integrated on CMOS. *Nature* **615**, 823–829 (2023).
69. D. Nishioka, T. Tsuchiya, T. Higuchi, K. Terabe, Enhanced synaptic characteristics of H_xWO_3-based neuromorphic devices, achieved by current pulse control, for artificial neural networks. *Neuromorphic. Comput. Eng.* **3**, 034008 (2023).
70. T. Tsuchiya, S. Miyoshi, Y. Yamashita, H. Yoshikawa, K. Terabe, K. Kobayashi, S. Yamaguchi, Direct observation of redox state modulation at carbon/amorphous tantalum oxide thin film hetero-interface probed by means of in situ hard X-ray photoemission spectroscopy. *Solid State Ion.* **253**, 110–118 (2013).
71. T. Tsuchiya, M. Imura, Y. Koide, K. Terabe, Magnetic control of magneto-electrochemical cell and electric double layer transistor. *Sci. Rep.* **7**, 10534 (2017).
72. T. Tsuchiya, S. Miyoshi, Y. Yamashita, H. Yoshikawa, K. Terabe, K. Kobayashi, S. Yamaguchi, Room temperature redox reaction by oxide ion migration at carbon/Gd-doped CeO2 heterointerface probed by an in situ hard x-ray photoemission and soft x-ray absorption spectroscopies. *Sci. Technol. Adv. Mater.* **14**, 045001 (2013).
73. K. Terabe, T. Tsuchiya, R. Yang, M. Aono, Nanoionic devices enabling a multitude of new features. *Nanoscale* **8**, 13873–13879 (2016).
74. D. Nishioka, T. Tsuchiya, T. Higuchi, K. Terabe, Oxygen-tolerant operation of all-solid-state ionic-gating devices: Advantage of all-solid-state structure for ionic-gating. *Jpn. J. Appl. Phys.* **59**, SIIG09 (2020).
75. J. Song, K. Kawakami, K. Ariga, Nanoarchitectonics in combat against bacterial infection using molecular, interfacial, and material tools. *Curr. Opin. Colloid Interface Sci.* **65**, 101702 (2023).
76. M. Matsumoto, L. Sutrisno, K. Ariga, Covalent nanoarchitectonics: Polymer synthesis with designer structures and sequences. *J. Polym. Sci.* **61**, 861–869 (2023).
77. K. Ariga, Molecular machines and microrobots: Nanoarchitectonics developments and on-water performances. *Micromachines* **14**, 25 (2023).
78. T. Tsuchiya, T. Nakayama, K. Ariga, Nanoarchitectonics intelligence with atomic switch and neuromorphic network system. *Appl. Phys. Express* **15**, 100101 (2022).
79. T. Tsuchiya, K. Terabe, R. Yang, M. Aono, Nanoionic devices: Interface nanoarchitechtonics for physical property tuning and enhancement. *Jpn. J. Appl. Phys.* **55**, 1102A4 (2016).

Acknowledgments

Funding: This work was supported by Japan Society for the Promotion of Science (JSPS) KAKENHI Grant Number JP22H04625 (Grant-in-Aid for Scientific Research on Innovative Areas "Interface Ionics"), Japan Society for the Promotion of Science (JSPS) KAKENHI Grant Number JP22KJ2799 (Grant-in-Aid for JSPS Fellows), JST PRESTO (grant number, JPMJPR23H4), and the Iketani Science and Technology Foundation. **Author contributions:** D.N., Y.S., T.T., and K.T. conceived the idea for the study. D.N., Y.S., and T.T. designed the experiments. D.N., Y.S., and T.T. wrote the paper. D.N. and Y.S. carried out the experiments. Y.S. prepared the samples. D.N., Y.S., and T.T. analyzed the data. All authors discussed the results and commented on the manuscript. K.T. directed the projects. **Competing interests:** The authors declare that they have no competing interests. **Data and materials availability:** All data needed to evaluate the conclusions in the paper are present in the paper and/or the Supplementary Materials.

Submitted 2 September 2023
Accepted 23 January 2024
Published 28 February 2024
10.1126/sciadv.adk6438